Hydrological Processes

WILEY

RESEARCH ARTICLE OPEN ACCESS

A Novel Framework for Estimating the Bowen Ratio Over Small Water Bodies

Amir Rezazadeh[1] | Pooria Akbarzadeh[1,2] | Mohammad Mohsen ShahMardan[1] | Milad Aminzadeh[3]

[1]Faculty of Mechanical Engineering, Shahrood University of Technology, Shahrood, Iran | [2]Institute of Fluid Mechanics and Heat Transfer, Johannes Kepler University Linz, Linz, Austria | [3]Institute of Geo-Hydroinformatics, Hamburg University of Technology, Hamburg, Germany

Correspondence: Pooria Akbarzadeh (akbarzad@ut.ac.ir; pooria.akbarzadeh@jku.at)

Received: 10 July 2024 | **Revised:** 24 December 2024 | **Accepted:** 29 December 2024

Funding: The authors received no specific funding for this work.

Keywords: Bowen ratio | latent heat flux | sensible heat flux | water reservoirs | water surface flow

ABSTRACT

The Bowen ratio, defined as the ratio of sensible to latent heat flux, is crucial for quantifying land-atmosphere energy exchanges and evaporation rates from terrestrial surfaces. Despite extensive research on the Bowen ratio over placid water surfaces (e.g., lakes), further investigation is needed to understand its dynamics in small reservoirs subjected to water inflow/outflow (i.e., surface flows) and wind. To address this knowledge gap, the evaporation rate and the sensible heat exchanges are measured between the water surface and overlying air in a small laboratory basin under different water surface flow rates ($1.0\text{–}10.5\,\mathrm{l\,min^{-1}}$) and wind speeds ($0\text{–}2.0\,\mathrm{m\,s^{-1}}$). Three different wind flow conditions are explored: no wind, headwind (opposing the water surface flow), and tailwind (aligning with water surface flow). The findings indicate strong correlations between sensible heat flux, water surface flow rate, and wind speed, particularly under headwind conditions. Nevertheless, concerning the latent heat flux, the measurements demonstrate that for each wind condition, the evaporation reaches its minimum value in a certain water surface flow rate, resulting in the highest value of the Bowen ratio. To facilitate the application of these laboratory findings for estimating the Bowen ratio under real environmental conditions, mathematical relationships using dimensionless numbers obtained through non-linear regression analysis are established. The results exhibit a good agreement with measurements in a small water basin.

1 | Introduction

Quantifying dynamics of the Bowen ratio (the ratio of sensible heat flux, H, to latent heat flux, LE) over water surfaces is crucial for understanding land-atmosphere energy exchanges, local climatic patterns, and evaporation mass loss rates (Kalma and Jupp 1990; Aminzadeh, Lehmann, and Or 2018; Aminzadeh et al. 2024; Millán, Estrela, and Caselles 1995; Yang and Lau 2004). Accurate estimation of the Bowen ratio requires simultaneous determination of H and LE, which are influenced by various surface and atmospheric factors such as temperature, atmospheric instability, wind speed, and surface roughness (Goldbach and Kuttler 2015; Verburg and Antenucci 2010).

The seminal work of Priestley and Taylor (1972) established a reliable framework, referred to here as the PT model, for estimating the Bowen ratio over extensive, placid water surfaces (e.g., oceans) under advection-free conditions. The PT model is particularly effective for large wet surfaces characterised by high relative humidity and dense vegetation cover, typically associated with a positive Bowen ratio (Yang and Roderick 2019). However, in natural conditions, water reservoirs are often subjected to wind and surface flows that dynamically affect surface roughness and induce mixing within the water body. These factors can result in scenarios where the assumptions of the PT model are violated, particularly in cases of strong advection or negative Bowen ratios. Consequently, the PT model may yield unreliable results in arid or semi-arid regions, areas experiencing significant advection, or when the water surface temperature is lower than the air temperature (Arasteh and Tajrishy 2008; Rohli et al. 2004; Majidi et al. 2015; Aminzadeh and Or 2014).

Direct estimates of the Bowen ratio benefit from the high-frequency measurements of vertical turbulent fluxes by the Eddy Covariance (EC) system assessing the covariance between vertical wind speed, vapour concentration, and temperature fluctuations. The EC system is widely recognised as a valuable and reliable approach, often serving as a reference for validating the accuracy of other methods (Yao et al. 2013; Sun et al. 2018; Nordbo et al. 2011). Despite the wide application of the EC system for the determination of the Bowen ratio over large water bodies (Moreo and Swancar 2013; Yao et al. 2014), its measurements over small water reservoirs might be affected by the footprint of surface fluxes originating from surrounding land surfaces (McJannet et al. 2011; McGloin et al. 2014).

The energy balance equation (Appendix D), which includes various quantities such as net radiation (R_n), the heat stored (ΔS) in water, the heat transfer rate through the flow of water (Q_V) and sensible and latent heat fluxes, can be an alternative approach to calculating the Bowen ratio (Cooley 1970; Aminzadeh and Or 2014). However, it is evident that some of the mentioned parameters, specifically the heat stored, which depends on the temperature of water layers, may not be easily available or measured.

The existing knowledge gap is in accurately determining the Bowen ratio over small water reservoirs, particularly when facing water surface flows and wind speeds. These factors can lead to the thermal mixing of water layers, influencing energy exchange at the water-air interface and thus surface fluxes. Hence, the primary objective of this study is to propose a physical framework for estimating the Bowen ratio in small water reservoirs, considering the influence of surface flows and wind. Employing well-controlled laboratory experiments and physical modelling, this study formulates the Bowen ratio through non-linear regression, employing effective dimensionless numbers.

2 | Materials and Methods

This section begins with an introduction to the main equipment, the test rig, and the test protocols. Subsequently, influential variables are identified and categorised as dimensionless numbers. These dimensionless parameters will guide the devising of appropriate regression equations for reliable estimates of the Bowen ratio under various environmental conditions (Section 3.2). The section concludes by presenting the characteristics of a small agricultural reservoir, where the performance of the regression equations is to be assessed and compared with the measured results.

2.1 | Test Equipment and Experimental Procedure

The experiments are conducted in a polyethylene basin with a surface area of $107 \times 107\,\mathrm{cm}^2$, a depth of 50 cm, and a wall thickness of 6 mm (Figure 1). To establish water surface flows, a centrifugal pump is used to create seven different flow rates: $1, 2.5, 4.5, 5.5, 7.5, 8.5$, and $10.5\,\mathrm{l\,min}^{-1}$. A Mariotte bottle maintains a constant water level in the basin in the presence of surface flow. Two parallel fans generate a uniform wind flow above the water surface with speeds of $1.4, 1.55, 1.7, 1.85$ and $2\ \mathrm{m\ s} - 1$. The evaporative loss is determined by measuring the water weight in the Mariotte bottle using a load cell (Zemic: 30 kg, L6N c3: ±3.45 g & ±0.0230% FS accuracy, China). To monitor the laboratory environmental conditions, a multifunctional transmitter (KIMO−C310: ±1.5% FS—RH & ±3.05% FS–Vel accuracy, France) is employed. This transmitter is capable of measuring relative humidity and wind speed. The humidity sensor and the anemometer of the transmitter are situated 20 and 30 cm above the water surface, respectively. Additionally, the air temperature above the water surface is measured using three temperature sensors positioned at heights of $z_1 = 0.4$, $z_2 = 10$ and $z_3 = 20$ cm. The vertical water temperature profile is monitored using an array of six thermocouples (KTT320, KIMO: $\pm 0.1^{\circ}$C accuracy, France). These thermocouples are fixed at depths of $\mathrm{Z_w} = 0$, $Z_{M1} = 7$, $Z_{M2} = 14$, $Z_{M3} = 21$, $Z_{M4} = 28$, and $Z_B = 35$ cm below the water surface. Additionally, some thermocouples are installed on the side walls and bottom of the basin to measure their respective temperatures. For measuring the heat flux in the water-air interface, a heat-flux sensor (FHF01, Hukseflux: $-1000 \sim +1000\ \mathrm{W\,m}^{-2}$, $\pm 5\ \mathrm{W\,m}^{-2}$ accuracy, Netherlands) is used. This sensor includes an integrated temperature sensor, which is commonly utilised by connecting one of its sides to a solid object. This study aims to apply this sensor to measure sensible heat flux at the air-water interface where both sides are in contact with the fluid. To do this, the sensor is installed tangentially to the water surface. This ensures that the lower part of the sensor remains in constant contact with the water surface while the upper part is exposed to the airflow passing over the water surface. The reliability of the sensible heat flux measurements obtained with the heat flux sensor is assessed through the energy balance approach, which is detailed in Appendix D. In order to provide a relatively uniform radiation flux over the surface, six 500 W OSRAM lamps are utilised. The average shortwave radiation across the surface of the basin is approximately $480\ \mathrm{W\,m}^{-2}$, which is measured using a solarimeter (SL100 KIMO: $0 - 1300\ \mathrm{W\,m}^{-2}$, $\pm 50\ \mathrm{W\,m}^{-2}$ accuracy, France). It is important to note that the tungsten-halogen spectrum closely resembles the sunlight spectrum, with a peak at $0.9\ \mu$m at a temperature of 3200 K. The first 5 h of each test are allocated to establishing an approximate equilibrium in environmental conditions, encompassing air temperature and relative humidity as measured by all relevant sensors. The final hour is dedicated solely to recording the collected data. Generally, tests are conducted under three main conditions: no wind, headwind (opposing the water surface flow), and tailwind (aligning with the water surface flow). During each test, the sensible heat is measured continuously for 6 h. For the sake of simplifying the representation of test conditions, the symbol S_x^q is identified such that q denotes the water surface flow rate [$\mathrm{l\,min}^{-1}$], and x represents the wind speed [$\mathrm{m\,s}^{-1}$].

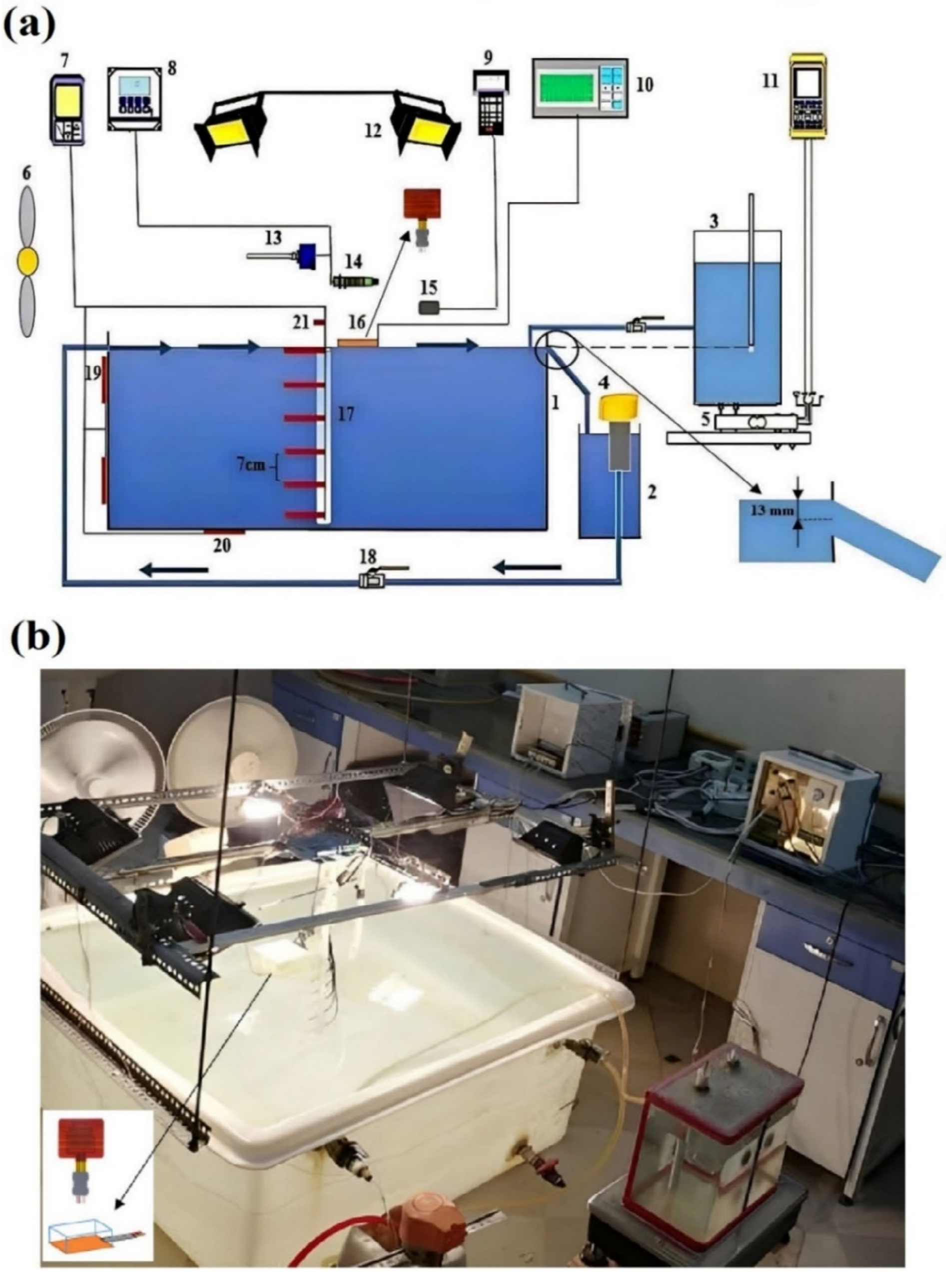

FIGURE 1 | (a) Schematic drawing of the equipment and setup: (1) polyethylene basin, (2) pump reservoir, (3) Mariotte bottle, (4) pump, (5) load cell, (6) fan, (7) thermometer, (8) multifunctional transmitter, (9) solarimeter, (10) the heat flux sensor data logger, (11) load data logger, (12) lamps, (13) wind speed sensor, (14) the air temperature and humidity sensor, (15) radiation sensor, (16) the heat flux sensor, (17) thermocouples, (18) valve, (19) wall temperature thermocouple, (20) floor temperature thermocouple, (21) thermocouple. (b) The actual photograph of the laboratory equipment in the case the wind direction is aligned with the surface water flow (tailwind).

2.2 | Dimensional Analysis and Identification of Effective Parameters

Considering that the Bowen ratio relies on heat and mass transfer mechanisms, it is affected by several variables. In the current experimental study, these variables include the speed of water surface flow (U_w), wind speed (U_a), net radiation (R_n), the temperature difference between the air and water surfaces (ΔT), air density (ρ_a), water density (ρ_w), the specific heat capacity of air (c_p), the dynamic viscosity of air (μ_a), the dynamic viscosity of water (μ_w), the thermal diffusion coefficient of air (α_a), the thermal diffusion coefficient of water (α_w), the characteristic length of the reservoir for wind (l_a), the hydraulic length of the reservoir for water surface flow (l_w), and the ratio of air gravity acceleration to air temperature (ϕ). Table 1 displays the dimensions of the quantities impacting the Bowen ratio. The quantities that are shared between air and water are denoted by the index "i" in Table 1. By considering Table 1 as a matrix, its rank would be four. Meanwhile, the total number of defined quantities is nine. Thus, five dimensionless numbers from Table 1 should be extracted for further analysis and interpretation.

TABLE 1 | The dimensions of the quantities impacting sensible and latent heat flux.

Dim	l_i	U_i	c_{p_i}	ΔT	μ_i	ρ_i	ϕ	α_i	R_n
M	0	0	0	0	1	1	0	0	1
L	1	1	2	0	−1	−3	1	2	0
t	0	−1	−2	0	−1	0	−2	−1	−3
T	0	0	−1	1	0	0	−1	0	0

The first dimensionless number is the Prandtl, representing the ratio between momentum and thermal diffusivity. For air and water, the Prandtl number can be expressed as follows, respectively:

$$\mathrm{Pr_a} = \frac{\rho_a}{\mu_a \alpha_a} \tag{1}$$

$$\mathrm{Pr_w} = \frac{\rho_w}{\mu_w \alpha_w} \tag{2}$$

The Rayleigh number, the second dimensionless number, which describes the relationship between momentum and thermal diffusivity, is defined for air as follows:

$$\mathrm{Ra} = \frac{\rho_a \phi}{\mu_a \alpha_a} (\Delta T) {l_a}^3 \tag{3}$$

here, l_a represents the ratio of the area to the reservoir's perimeter, which is equal to 0.267 m for the basin used in the current study. The Reynolds number, representing the ratio between inertial and viscous forces, is the third dimensionless number. For airflow, the Reynolds number can be calculated using Equation (4), while for water flow, it can be determined using Equation (5):

$$\mathrm{Re}_a = \frac{\rho_a U_a l_a}{\mu_a} \tag{4}$$

$$\mathrm{Re}_w = \frac{\rho_w U_w l_w}{\mu_w} \tag{5}$$

Here, U_w and l_w are obtained from Equations (6) and (7), respectively:

$$U_w = \frac{q}{A_V} \tag{6}$$

$$l_w = \frac{4A_V}{p} \tag{7}$$

where, A_V is the cross-sectional area perpendicular to the water surface flow ($1.07 \times 0.013\,\mathrm{m}^2$) and p is the perimeter of the surface flow ($2 \times [1.07 + 0.013] = 2.166\,\mathrm{m}$). This yields $l_w = 0.025\ m$. The fourth dimensionless number is the Eckert number, which characterises the relationship between the kinetic energy of the flow and the boundary layer enthalpy difference:

$$\mathrm{Ec} = \frac{{U_a}^2}{c_p \Delta T} \tag{8}$$

The final dimensionless number, which considers net radiation, air density, and wind speed, is represented by Equation (9):

$$\phi_R = \frac{R_n}{\rho_a {U_a}^3} \tag{9}$$

2.3 | A Small Agricultural Reservoir in Real Environmental Conditions

In this study, the measurements of Bakhtiar et al. (2022) in a small agricultural reservoir in Isfahan, Iran (E 51°31′, N 32°42′), with a surface area of 25 m^2 and depth of 2 m are used to evaluate estimates of the Bowen ratio under natural field conditions. The experimental data includes the radiation, wind speed, vertical temperature of water layers, surface evaporation rate, and relative humidity from April 2019 to March 2020 (Bakhtiar et al. 2022). This reservoir has no surface flow, so the Reynolds number is assumed to be zero. Due to the lack of direct measurement of sensible heat flux, we calculated it using the energy balance equation (Appendix D) and determined the Bowen ratio based on the available surface evaporation rates.

3 | Results

3.1 | Experimental Measurements and Observations

This section begins by outlining the laboratory environmental conditions during the experiments, focusing on air temperature and relative humidity (Section 3.1.1). Following this, Section 3.2.1 addresses the uncertainties associated with the sensible heat flux, evaporation rate, and the Bowen ratio. The effects of water surface flow rate and wind speed on the temperature of water layers, sensible heat flux, and evaporation rate are examined in Sections 3.1.3–3.1.5, respectively.

3.1.1 | Equilibrium Ambient Conditions

The experiments are carefully planned to ensure well-controlled laboratory and environmental equilibrium conditions. To illustrate this (Appendix A), Figure A1 displays the relative humidity [%] and Figure A2 shows the air temperature [°C] above the basin's surface recorded by the respective sensors. The figures display the data for six distinct cases: $S_{0.0}^{0.0}$, $S_{1.4}^{0.0}$, $S_{1.55}^{0.0}$, $S_{1.7}^{0.0}$, $S_{1.85}^{0.0}$ and $S_{2.0}^{0.0}$, representing the last hour of each test. The figures show that the relative humidity and air temperature remain relatively constant during the specified period. This condition holds for most water surface flows and wind speeds.

3.1.2 | Uncertainty Analysis

In this study, each test is conducted three times, and the average values of these replications are utilised for further analysis. The standard error, calculated by dividing the standard deviation by the square root of the number of measurements, is expressed as uncertainty. The uncertainty values for the evaporation rate are shown in Figure 4 (Section 3.1.5) for all the different water surface flows and wind speeds. To maintain clarity in the graphs, the uncertainty for sensible heat flux (Figure 2 in Section 3.1.4) and the Bowen ratio (Figure 5 in Section 3.2) is explicitly emphasised only at $U_a = 0\ \mathrm{m\ s^{-1}}$, while the remaining wind speeds present the average values without uncertainty to avoid confusion. Appendix B gives full details of uncertainty values for sensible heat flux (Table B1) and the Bowen ratio (Table B2). These uncertainties may arise due to challenges in achieving equilibrium environmental conditions during the tests and the inherent accuracy limitations of the measurement devices.

3.1.3 | Vertical Water Temperature Profile

Due to the interception of radiative flux, the surface of a water body often experiences a higher temperature relative to the subsurface layers. This leads to a low-density layer on the water surface, known as the epilimnion layer (Rezazadeh, Akbarzadeh, and Aminzadeh 2020a, 2020b). The epilimnion acts as a barrier, hindering mass and energy transfer into the lower layers, known as the hypolimnion layers. The thermal stratification adversely affecting the water quality and thus aquatic life (Van Dijk and Van Vuuren 2009) can be alleviated by the thermal mixing of the layers by surface flows. Figure C1 in Appendix C illustrates the temperature changes in six water layers for the tailwind cases. The data presented are from the last hour of experiments conducted for the states $S^{0.0}_{0.0}$ (Figure C1a), $S^{0.0}_{2.0}$ (Figure C1b), $S^{4.5}_{0.0}$ (Figure C1c), $S^{4.5}_{2.0}$ (Figure C1d), $S^{10.5}_{0.0}$ (Figure C1e), $S^{10.5}_{2.0}$ (Figure C1f). Figure C2 showcases the temperature changes for the headwind case, specifically for the states of $S^{1.0}_{1.4}$ (Figure C2a), $S^{1.0}_{2.0}$ (Figure C2b), $S^{4.5}_{1.4}$ (Figure C2c), $S^{4.5}_{2.0}$ (Figure C2d), $S^{10.5}_{1.4}$ (Figure C2e) and $S^{10.5}_{2.0}$ (Figure C2f). In both figures, T_w represents the water surface temperature, while T_{M1}, T_{M2}, T_{M3}, T_{M4} and T_B represent the water temperatures at depths $Z_w = 0$, $Z_{M1} = 7$, $Z_{M2} = 14$, $Z_{M3} = 21$, $Z_{M4} = 28$ and $Z_B = 35$ cm, respectively. Both figures provide compelling evidence of thermal mixing among the water layers due to surface flow and wind speed. For instance, in the $S^{0.0}_{0.0}$ state,

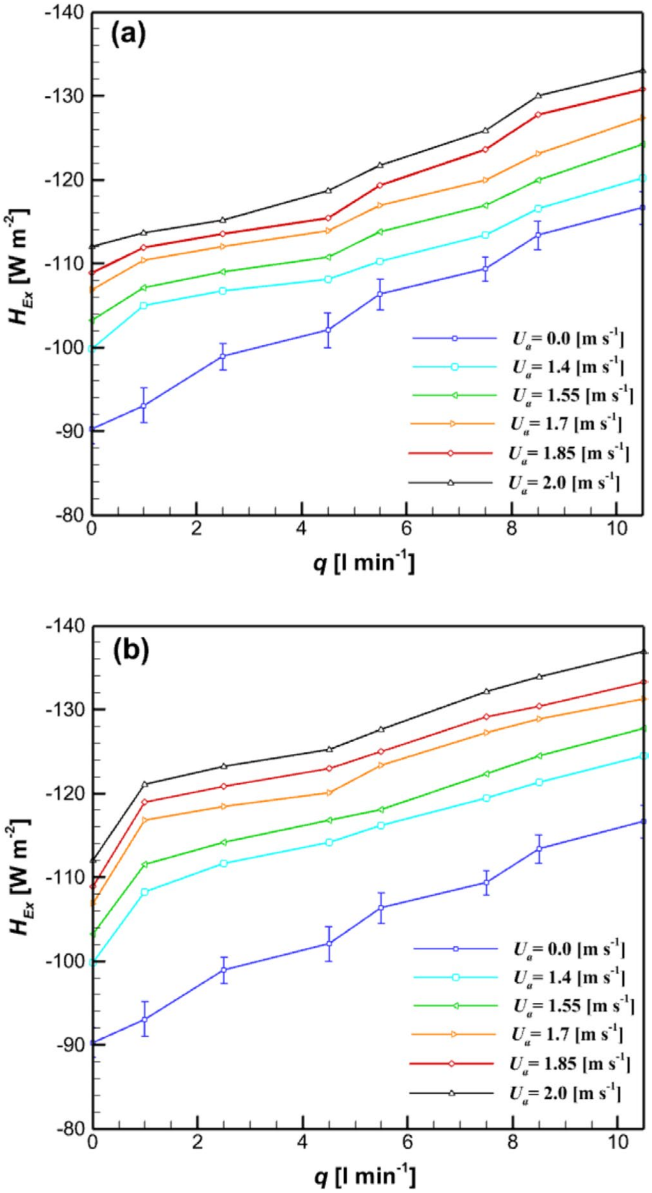

FIGURE 2 | Sensible heat flux measured by the heat flux sensor at the air-water interface: (a) Tailwind. (b) Headwind.

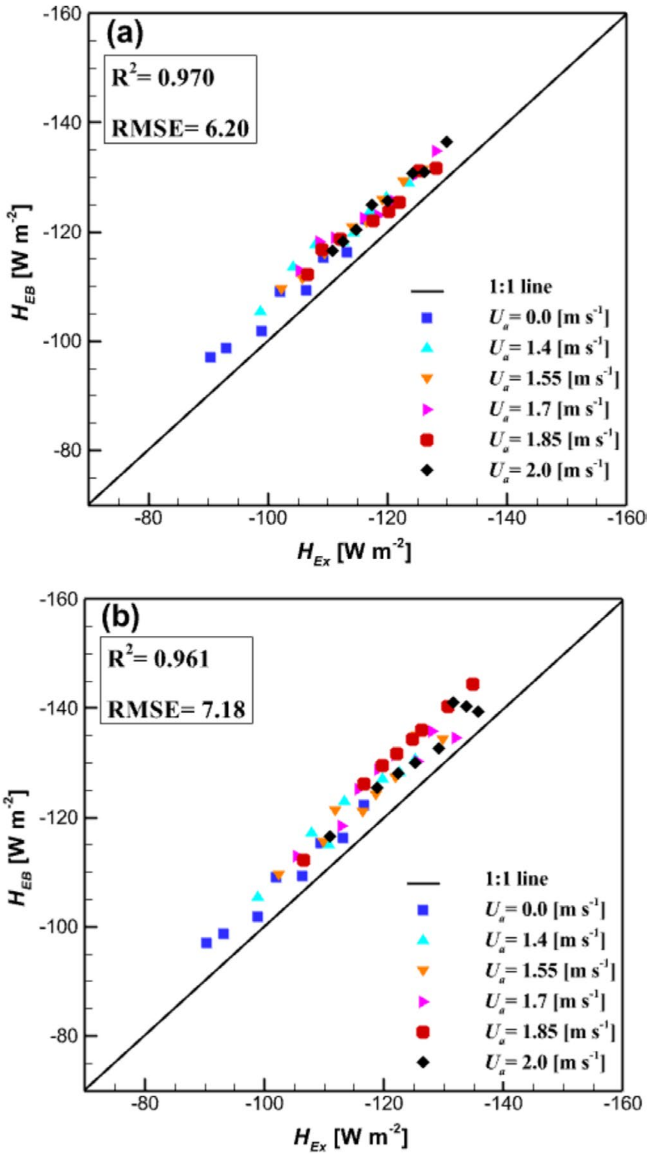

FIGURE 3 | Comparison between the values of sensible heat flux measured by the heat flux sensor (H_{Ex}) and calculated based on the energy balance equation (H_{EB}): (a) Tailwind, (b) Headwind.

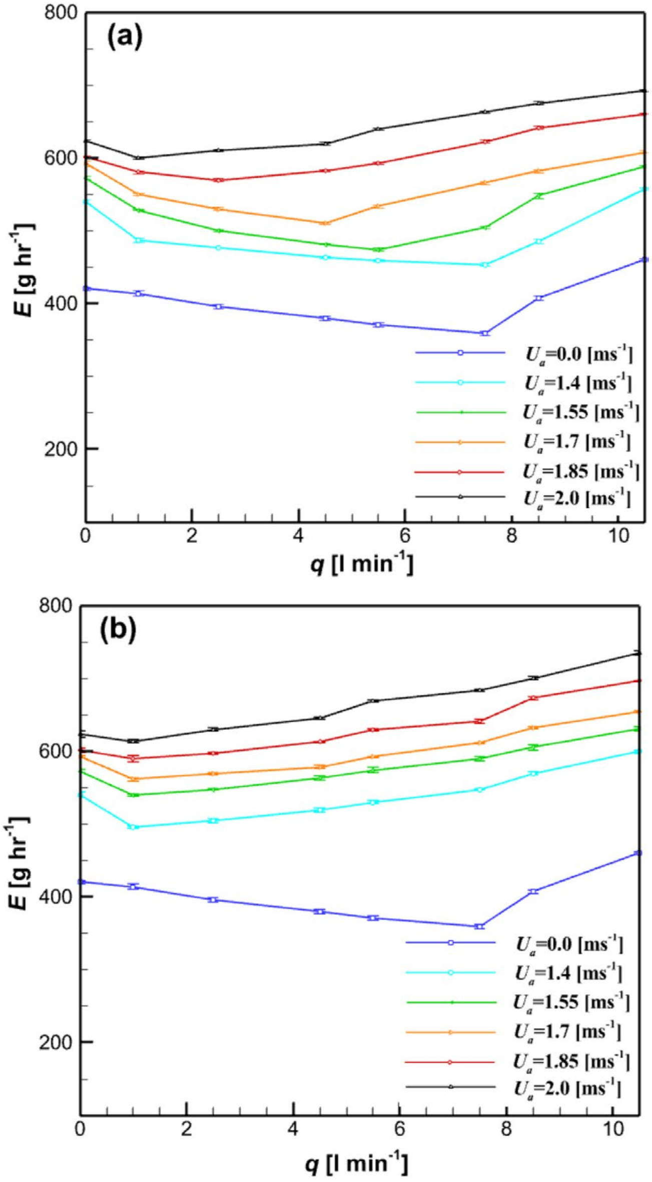

FIGURE 4 | The experimental results of water evaporation rate (E) for different water surface flows and wind speeds: (a) Tailwind, (b) Headwind.

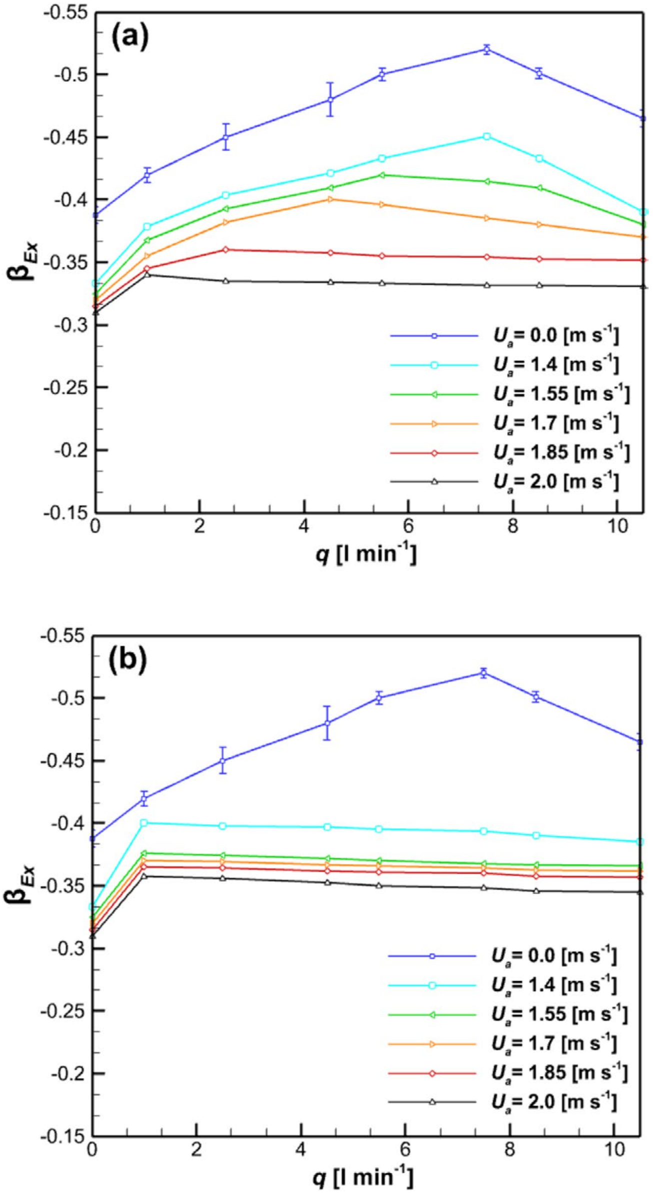

FIGURE 5 | The experimental results of the Bowen ratio ($\beta_{Ex} = H_{Ex} / LE_{Ex}$) in the laboratory reservoir for different water surface flows and wind speeds: (a) Tailwind; (b) Headwind.

thermal stratification is evident. On the other hand, the $S_{2.0}^{10.5}$ state demonstrates closely aligned temperatures across the six water layers. Furthermore, it can be observed that in the headwind case, the degree of thermal mixing among the layers increases. For example, in Figure C2, the $S_{2.0}^{10.5}$ state shows significantly similar temperatures across the six water layers compared to the $S_{2.0}^{10.5}$ state depicted in Figure C1.

3.1.4 | Sensible Heat Flux in the Presence of Water Surface Flow and Wind Speed

Figure 2 illustrates the results of the sensible heat measurements obtained using the heat flux sensor at the air-water interface (H_{Ex} $[\mathrm{W\,m^{-2}}]$) in tailwind (Figure 2a) and headwind (Figure 2b) scenarios. The water surface flows are selected as 0 (denoted as the reference state), 1, 2.5, 4.5, 5.5, 7.5, 8.5, and 10.5 $\mathrm{l\,min^{-1}}$ and the wind speeds are considered as 0.0, 1.4, 1.55, 1.7, 1.85, and 2 $\mathrm{m\,s^{-1}}$. As shown in Figure 2, the sensible heat flux increases by increasing the water surface flow and wind speed. For example, in the case of tailwind (Figure 2a), an increase of about 47% is observed in $S_{2.0}^{10.5}$ compared to the case of $S_{0.0}^{0.0}$ (no wind, no water surface flow). In this regard, Figure 2b reveals that in headwind scenarios, the increase in sensible heat flux is slightly more significant than in tailwind scenarios. So that, in the case of $S_{2.0}^{10.5}$, the increase in sensible heat flux is about 52% compared to the case of $S_{0.0}^{0.0}$.

Here, it is imperative to assess the accuracy of utilising the heat flux sensor in measuring the value of sensible heat exchanges. To achieve this, the sensible heat flux is also calculated using the energy balance equation as an alternative and well-established approach (see Appendix D for details). The resulting value for the sensible heat flux from this method is denoted as H_{EB}. Figure 3a,b depict a comparison between the outcomes of the heat flux sensor (H_{Ex}) and those derived from the energy balance equation (H_{EB}) under tailwind and headwind conditions, respectively. The consistency of results reflected in the coefficient of determination (R^2) and the root mean square error (RMSE) underscores the reliability of the heat flux sensor measurements (see Table E1 in Appendix E).

3.1.5 | Variation in Evaporation With Water Surface Flow and Wind Speed

Figure 4 illustrates the experimental results of the water surface evaporation during each test for tailwind and headwind cases. At the wind speed of $U_a = 0\ \mathrm{m\ s^{-1}}$ due to the thermal mixing of water layers caused by the water surface flows, the rate of evaporation decreases up to a certain flow rate, which is observed in the case of $S_{0.0}^{7.5}$. According to Figure 4a, it can be observed that until the wind speed reaches $1.4\ \mathrm{m\ s^{-1}}$, the thermal mixing of the layers has a reducing effect on surface evaporation up to the flow rate of $7.5\ \mathrm{l\ min^{-1}}$. As the wind speed increases, the flow rate of $7.5\ \mathrm{l\ min^{-1}}$ starts to retreat in reducing evaporation so that at a wind speed of $2\ \mathrm{m\ s^{-1}}$, the evaporation rate decreases to a flow rate of $1\ \mathrm{l\ min^{-1}}$. Figure 4b presents that in the cases of headwind, at all wind speeds, evaporation reduction occurs in the water flow rate of $1\ \mathrm{l\ min^{-1}}$. Also, as the flow rate increases, it can be seen from Figure 4b that the evaporation rate increases. Therefore, the effect of the thermal mixing of layers is evident in reducing evaporation only at a flow rate of $1\ \mathrm{l\ min^{-1}}$.

3.2 | Novel Bowen Ratio Formulations

Figure 5 shows the experimental results of the Bowen ratio ($\beta_{Ex} = H_{Ex} / LE_{Ex}$) in the laboratory reservoir for tailwind Figure 5a and headwind Figure 5b scenarios, encompassing various wind speeds and water surface flow rates. As indicated in the table, for tailwind scenarios, the case $S_{0.0}^{7.5}$ exhibits the highest value of the Bowen ratio, attributed to a reduction in evaporation (Figure 4). Conversely, in headwind scenarios, the highest Bowen ratio value is observed at a flow rate of $1\ \mathrm{l\ min^{-1}}$ (due to the greatest reduction in evaporation).

To facilitate and upscale the application of the laboratory findings for estimating the Bowen ratio in small water reservoirs, three mathematical relationships are established using dimensionless numbers, as detailed in Section 2.2. These relationships are derived through non-linear regression analysis. Approximately two-thirds of the data are employed for the training procedure (in SPSS software), while the remaining data are used to verify the accuracy of the regression formulas. For the no-wind scenarios, with 75% of the data designated as training, the following Bowen ratio formula is derived:

$$\beta_{Eq} = \left[e^{0.002(\mathrm{Re_w} - \mathrm{Pr_w})} + 2.107 e^{(t^* \mathrm{Pr_w})} - 8.982 \times 10^{-5} (t^* \mathrm{Ra})^{0.7} \right] \quad (10)$$

Here, t^* represents the ratio of the duration of recorded data for an experiment to the duration of 1 day. For instance, it equals 0.041 for 1 h and 0.5 for 12 h. In the scenarios of tailwind and no surface flow, 70% of the data is designated for training. Under these conditions, the regression analysis produces the following expression equation for the Bowen ratio:

$$\beta_{Eq} = 12.319 e^{\frac{-0.197\phi_R}{t^* \mathrm{Pr}^*}} - 11.849 e^{-\frac{\phi_R}{600 t^*}(\mathrm{Pr}^* - \mathrm{Ec})} - 0.288 e^{\frac{0.086}{\mathrm{Ec} - \mathrm{Re}^*}} \quad (11)$$

where $\mathrm{Pr}^* = \mathrm{Pr_w} / \mathrm{Pr_a}$ and $\mathrm{Re}^* = \mathrm{Re_w} / \mathrm{Re_a}$. For the headwind scenarios, 70% of the available data is utilised for training, yielding the following equation for the Bowen ratio:

$$\beta_{Eq} = 11.218 e^{\frac{-0.236\phi_R}{t^* \mathrm{Pr}^*}} - 10.665 e^{-\frac{\phi_R}{500 t^*}(\mathrm{Pr}^* - \mathrm{Ec})} - 0.32 e^{\frac{0.041}{\mathrm{Ec} - \mathrm{Re}^*}} \quad (12)$$

Figure 6a–c depict the comparison between the measured Bowen ratio (β_{Ex}), which are used as training data and values (β_{Eq}) obtained from Equations (10–12) for the no-wind, tailwind, and headwind scenarios, respectively. As can be seen from Figure 5, the R^2 values for the three scenarios are 0.956, 0.936, and 0.820, and the RMSE values are 0.009, 0.011, and 0.01, respectively.

3.2.1 | Verifying the Regression Equations by the Non-Training Laboratory Data

Figure 7 compares the Bowen ratio obtained from regression Equations (10–12) with the Bowen ratio obtained from the laboratory results (remaining non-training data). For the no-wind scenario, the cases $S_{0.0}^{2.5}$, $S_{0.0}^{8.5}$ (see Figure 6a), for the tailwind scenario, the cases $S_{1.4}^{1.0}$, $S_{1.4}^{2.5}$, $S_{1.55}^{0.0}$, $S_{1.55}^{7.5}$, $S_{1.7}^{0.0}$, $S_{1.7}^{8.5}$, $S_{1.7}^{10.5}$, $S_{1.85}^{4.5}$, $S_{1.85}^{7.5}$, $S_{2.0}^{1.0}$, $S_{2.0}^{5.5}$, $S_{2.0}^{10.5}$ (see Figure 6b), and for the headwind scenario, the cases $S_{1.4}^{4.5}$, $S_{1.4}^{5.5}$, $S_{1.55}^{0.0}$, $S_{1.55}^{8.5}$, $S_{1.55}^{10.5}$, $S_{1.7}^{1.0}$, $S_{1.7}^{4.5}$, $S_{1.85}^{2.5}$, $S_{1.85}^{5.5}$, $S_{2.0}^{1.0}$, $S_{2.0}^{7.5}$, $S_{2.0}^{10.5}$ (see Figure 6c) are selected for the verification data. In Figure 7a, the R^2 and RMSE values are 0.99 and 0.014, respectively. For Figure 7b, these values are 0.875 and 0.011, and for Figure 7c, they are 0.719 and 0.011.

3.2.2 | Evaluation of the Regression Equations Using Field Data

To assess the performance of the regression equations in real environmental conditions, an agricultural reservoir in Isfahan is chosen as a representative small basin. Figure 8 compares the daily average Bowen ratio obtained from the regression equations (β_{Eq}) with the measurements in the Isfahan agricultural reservoir (β_{EB}). This comparison is presented in two time intervals: 06: 00 AM – 06: 00 PM and 00: 00 AM – 24: 00 PM, from 1 August to 31 August 2019. Given that this reservoir lacks water surface flow, only Equations (11) and (12) are applicable to calculate β_{Eq}. Figure 8a,b represent β_{Eq} in connection with Equation (11), whereas Figure 8c,d depict β_{Eq} in relation to Equation (12). The Bowen ratio obtained from regression equations and the measured Bowen ratio (as shown in Figure 8) exhibit varying levels of agreement. Figure 8a shows an R^2 of 0.735 and an RMSE of 0.095. In Figure 8b, these values have an R^2 of 0.815 and an RMSE of 0.049. Figure 8c,d show R^2 values of 0.901 and 0.855, along with RMSE values of 0.070 and 0.044, respectively.

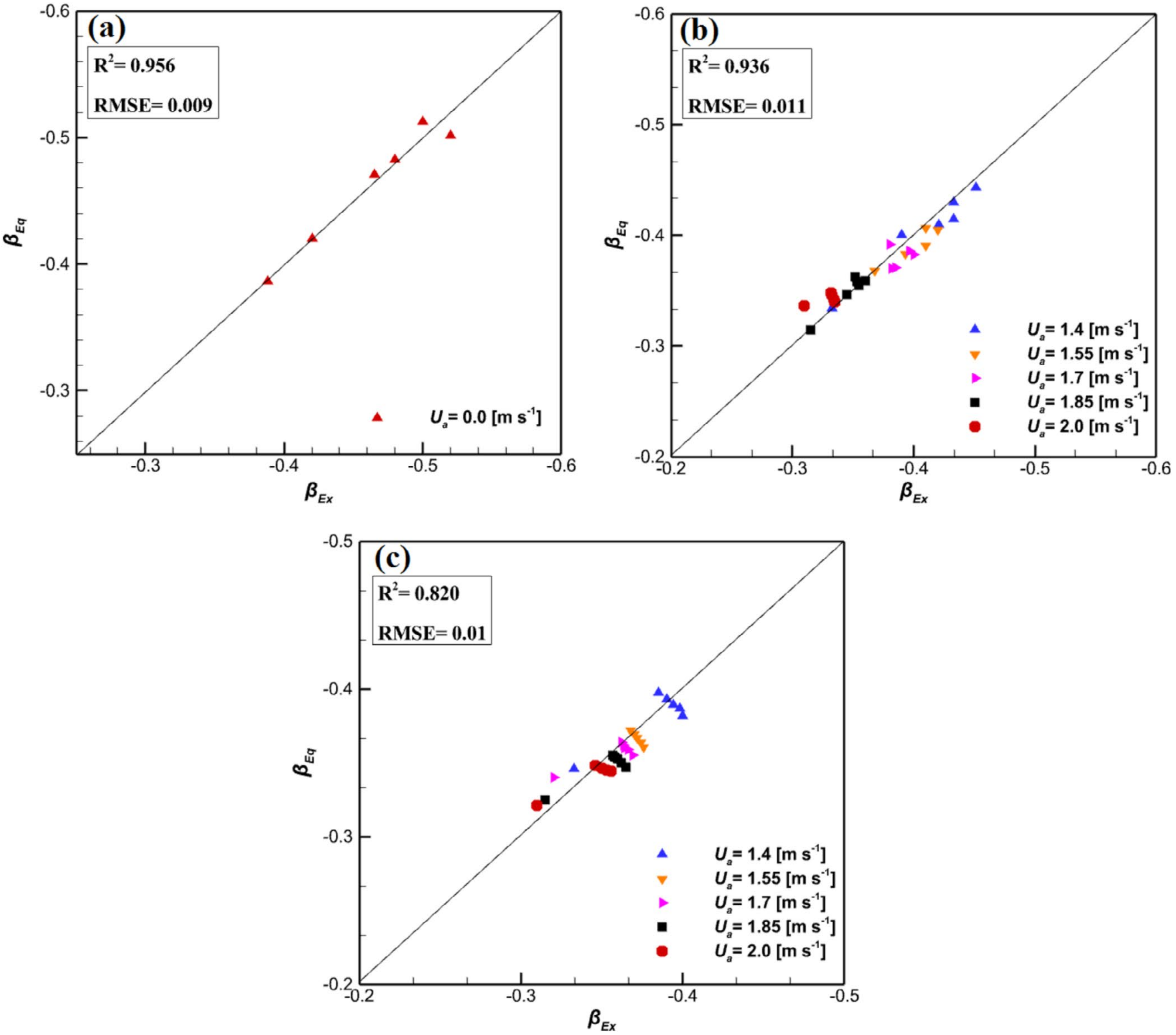

FIGURE 6 | The comparison between the measured Bowen ratio (β_{Ex}), which is used as training data, and the values obtained from regression equations (β_{Eq}): (a) No-wind, Equation (10). (b) Tailwind, Equation (11). (c) Headwind, Equation (12).

4 | Discussion

4.1 | The Effects of Water Surface Flow and Wind Speed on Sensible Heat Flux

As detailed in Sections 3.1.3 and 3.1.4, water surface flows and wind speeds play crucial roles in the thermal mixing of water layers, directly impacting sensible heat flux. Essentially, higher water surface flow and wind speed lead to increased sensible heat flux. For a clearer understanding, refer to Figure 9, which illustrates the average water surface temperature under varying water surface flows and wind speeds. Figure 9a depicts the scenario with the tailwind, while Figure 9b shows the scenario with the headwind. Water surface flows play a key role in mixing water layers and facilitating heat transfer from the surface to the lower layers. Consequently, this process leads to a decrease in the temperature of the water surface. The greater the rate of water surface flow, the more pronounced this temperature decrease becomes. For example, the average temperature of the water surface in the $S_{2.0}^{10.5}$ is lower than the $S_{2.0}^{1.0}$ condition. Since air temperature and relative humidity are almost uniform and identical in the two mentioned conditions, the decrease in the temperature of the water surface in the $S_{2.0}^{10.5}$ condition causes an increase in the temperature difference between the air and water surface and, as a result, an increase in the sensible heat flux compared to the $S_{2.0}^{1.0}$. In the case of headwind, due to more thermal mixing in the layers, the average temperature of the water surface has a lower value in all test conditions relative to the case of tailwind. For example, in the state $S_{1.4}^{1.0}$ of headwind, the average temperature of the water surface is about half a degree lower than the similar state in the tailwind. As a result of this event, the temperature difference between the surface of the water and the air near it, as well as the surface of heat transfer (due to the turbulence-induced roughness on the surface), increases and causes the value of sensible heat flux to increase compared to the tailwind.

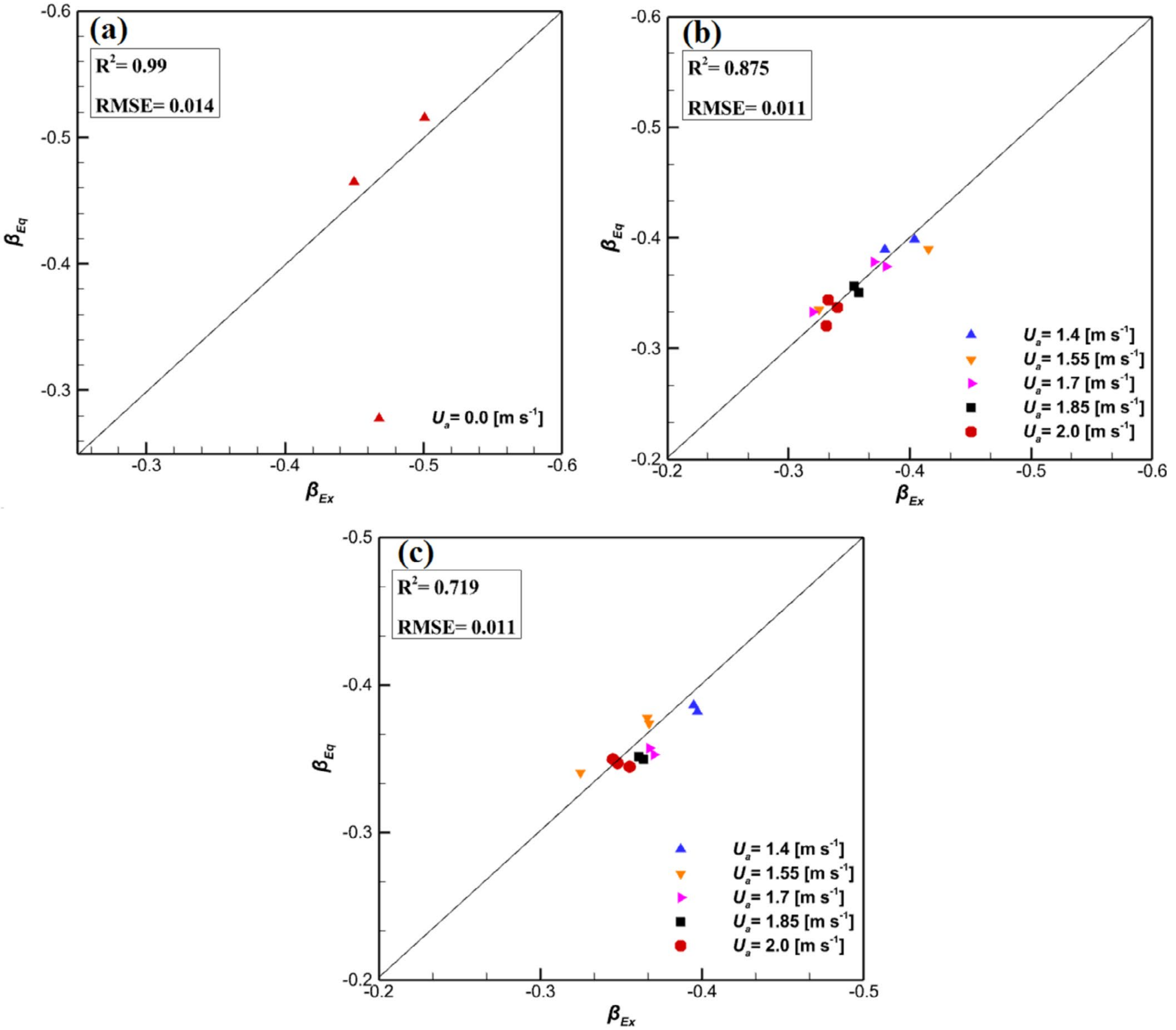

FIGURE 7 | The comparison between the Bowen ratio obtained from regression equations (β_{Eq}) with the Bowen ratio obtained from the laboratory results (remaining non-training data): (a) No-wind, Equation (10). (b) Tailwind, Equation (11). (c) Headwind, Equation (12).

4.2 | The Effects of Water Surface Flow and Wind Speed on Evaporation Dynamics

Several studies have linked the thermal mixing of water layers with a reduction in surface evaporation (Rachid et al. 2022; Youssef and Khodzinskaya 2019; Helfer et al. 2018; Sherman, Lemckert, and Zhang 2010). This evaporation reduction is estimated to be between 10 and 30% for small reservoirs in which thermal mixing is done by mechanical stirrers or inlet and outlet surface flows (Cox 1999; Rezazadeh, Akbarzadeh, and Aminzadeh 2020b). The thickness of the aerodynamic boundary layer and thermal mixing are critical factors influencing evaporation rates in these reservoirs. Surface flow creates an aerodynamic boundary layer whose thickness varies with the relative velocity between the water surface and the air. As surface flow increases, the thickness of this layer decreases, enhancing heat and vapour gradients between the water surface and the overlying air, thereby increasing evaporation and sensible heat fluxes (Haghighi and Or, 2013; Aminzadeh and Or 2014). As illustrated in Figure 4a, in the tailwind scenario, surface evaporation decreases up to a wind speed of 1.4 m s^{-1} and a flow rate of 7.5 l min^{-1}, indicating that thermal mixing is the dominant factor in reducing evapouration. Beyond a wind speed of 1.4 m s^{-1}, the flow rate of the reduction of evaporation retreats so that it has its lowest value at the wind speed of 2.0 m s^{-1}, so it is concluded that reducing the thickness of the aerodynamic boundary layer, which causes an increase in the sensible heat flux and evaporation, dominates the thermal mixing of the layers. Figure 4b shows that in headwind conditions, thermal mixing effectively reduces evaporation at all wind speeds up to a flow rate of 1.0 l min^{-1}. Beyond this flow rate, the impact of the thinner aerodynamic boundary layer becomes more significant, increasing the evaporation rate.

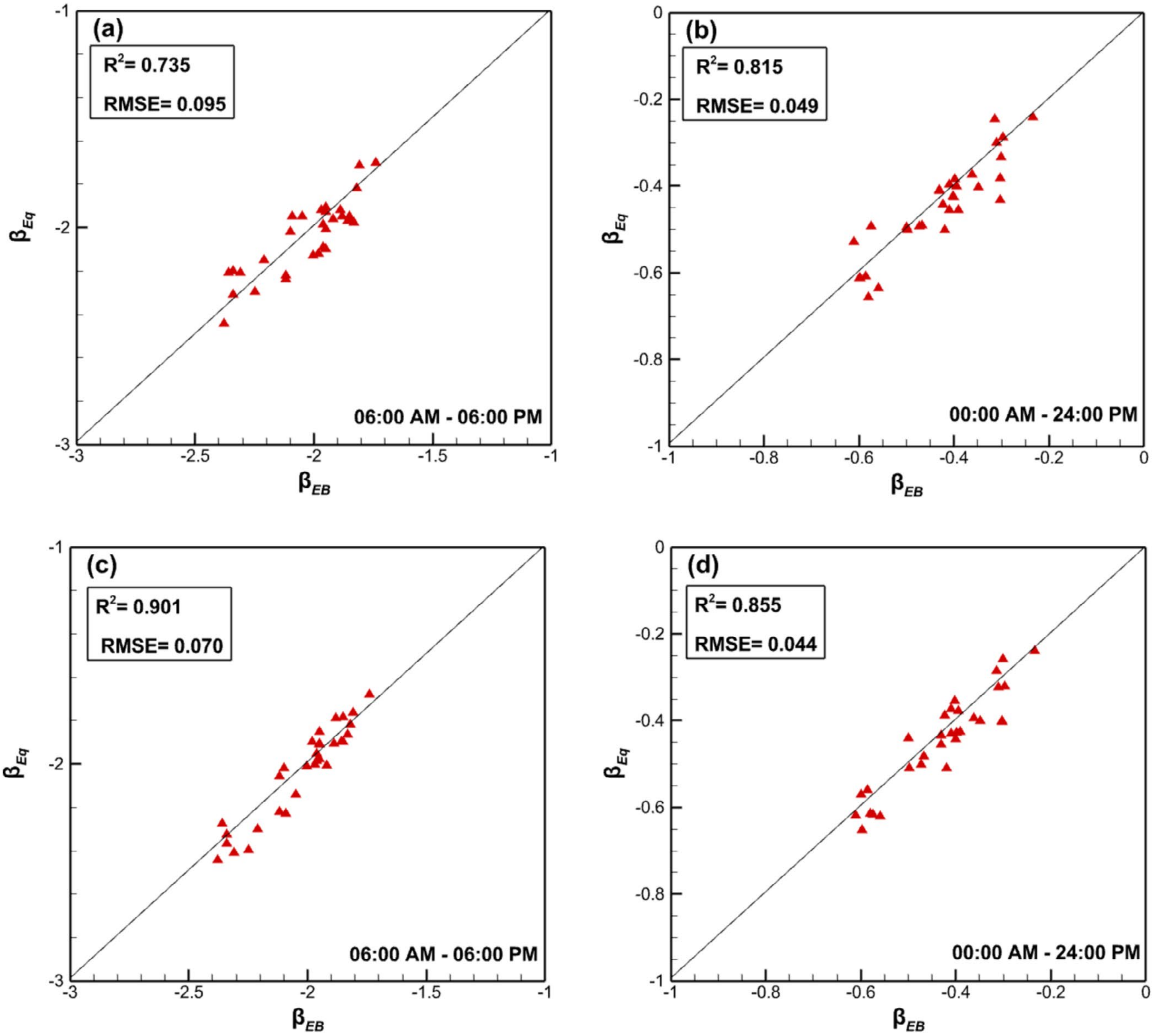

FIGURE 8 | Comparison of the daily average Bowen ratio obtained from regression equations (β_{Eq}) and the measurements in the agricultural reservoir (β_{EB}) from 1 August to 31 August 2019, for two different time intervals: (a) 06: 00 AM – 06: 00 PM, Equation (11). (b) 00: 00 AM – 24: 00 PM, Equation (11). (c) 06: 00 AM – 06: 00 PM, Equation (12). (d) 00: 00 AM – 24: 00 PM, Equation (12).

4.3 | The Performance of Regression Equations in the Assessment of the Bowen Ratio

Using the energy balance equation is one of the most common and standard methods for evaluating energy partitioning in water bodies (Cooley 1970; Aminzadeh and Or 2014). As mentioned in Sections 2.1 and 3.1.4, this study calculates sensible heat flux using the energy balance equation method alongside latent heat flux from load cell data to ensure the laboratory results for sensible heat flux are accurate (Figure 3). By accurately evaluating the latent and sensible heat fluxes and calculating the Bowen ratio (Section 3.2), the impact of various grouped variables on changes in the Bowen ratio can be determined through three equations corresponding to different conditions: no wind, tailwind, and headwind. Figures 6 and 7, along with their R^2 and RMSE values, confirm that the regression equations provide accurate estimates of the Bowen ratio under the given laboratory conditions for training and non-training data. According to Figure 8, which compares the performance of the regression equations (β_{Eq}) in calculating the Bowen ratio against measured values (β_{EB}), the regression equations demonstrate remarkable accuracy for the Bowen ratio estimation in the agricultural reservoir of Isfahan, which is subject to real environmental conditions.

4.4 | Limitations

The findings highlight the impact of water surface flows and wind speeds on variations in heat fluxes from small water reservoirs, providing reliable estimates of the Bowen ratio under three

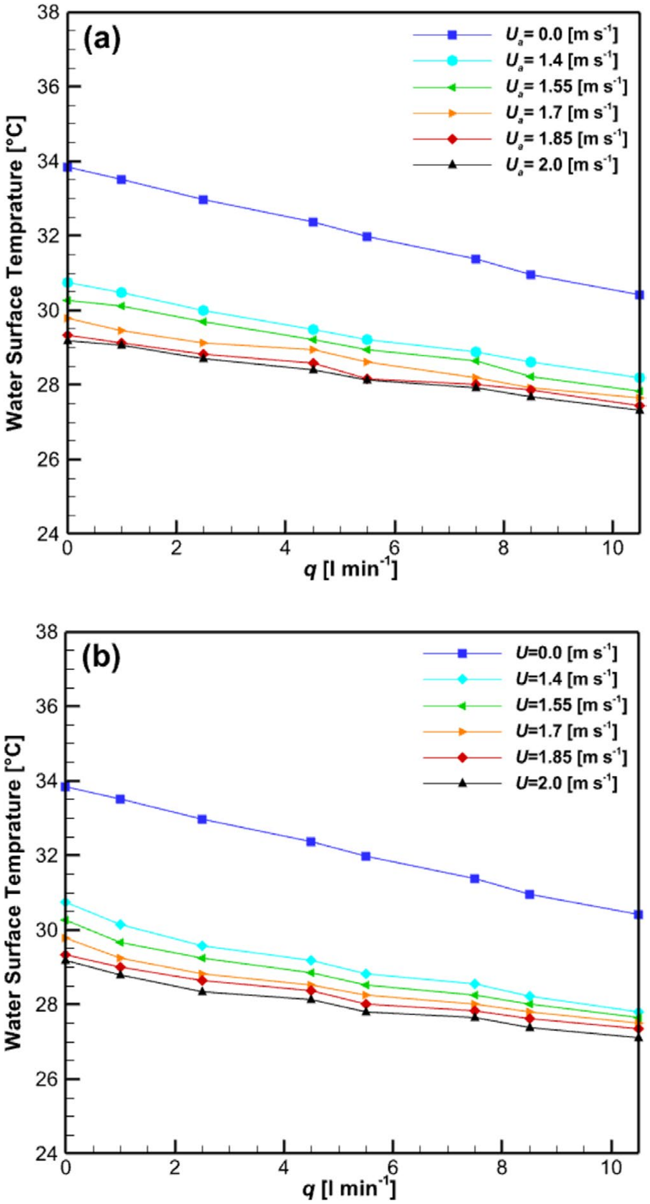

FIGURE 9 | The average water surface temperature for different water surface flows and wind speeds: (a) Tailwind, (b) Headwind.

distinct wind flow conditions: no wind, headwind (opposing the water surface flow), and tailwind (aligned with the water surface flow). This study emphasises cases where the sensible heat flux is directed from the air to the water surface due to the higher air temperature compared to the water surface temperature. However, in specific scenarios, such as when the water surface temperature exceeds the air temperature and water surface flows interact with crosswinds, the Bowen ratio derived from regression equations may become unreliable. Therefore, further investigations under these conditions are crucial to establishing a comprehensive physical framework for quantifying heat and mass transfer between water and atmospheric reservoirs.

5 | Summary and Conclusion

This study aims to investigate the Bowen ratio (the ratio of H to LE) in open small basins, considering the presence of water surface flows and wind speeds. The investigation encompasses laboratory tests and theoretical modelling. In terms of experimental analysis, a small water basin with a surface area of 1.14 m^2 and a depth of 0.5 m is utilised. The sensible heat flux is measured using a heat flux sensor, while the mass of evaporated water is measured using a load cell under varying water surface flows and wind speeds.

The results show that the sensible heat flux increases with the increase in surface water flow rate and wind speed. This increase is particularly significant when the wind direction is opposite to the water surface flow (headwind). When the wind direction aligns with the surface water flow direction (tailwind), the surface evaporation decreases as the water surface flow rate increases up to a certain wind speed. This decrease in evaporation persists until a specific surface flow rate (the so-called optimal flow rate) is reached, leading to the highest Bowen ratio. By passing the optimal flow rate, the evaporation rate gradually increases. However, once the wind speed surpasses a certain threshold, the optimal flow rate starts to decline due to thermal mixing and the impacts of the aerodynamic boundary layer. Regarding the headwind scenario, the optimal flow rate is at its lowest value across all tested conditions.

In the following, three novel Bowen ratio formulations are derived through nonlinear regression analysis using SPSS software for three conditions: no wind, tailwind, and headwind. This software treats the Bowen ratio as the dependent variable and dimensionless numbers as the independent variables. Approximately two-thirds of the data are employed for the software training procedure, while the remaining one-third are used to verify the accuracy of regression formulas. Additionally, the accuracy of these formulas is verified by data from a small agricultural reservoir. Both verifying approaches show excellent reliability for the regression equation.

Acknowledgements

The authors would like to acknowledge the Shahrood University of Technology for valuable support in different study aspects.

Ethics Statement

The authors declare that this work is original and has not been published elsewhere, nor is it currently under consideration for publication elsewhere. All research practices followed ethical guidelines appropriate to the study.

Consent

The authors grant the publisher permission to publish the work.

Conflicts of Interest

The authors declare no conflicts of interest.

Data Availability Statement

The data and model supporting the findings of this study can be obtained from the corresponding author upon reasonable request.

References

Ali, S., N. C. Ghosh, and R. Singh. 2008. "Evaluating Best Evaporation Estimate Model for Water Surface Evaporation in Semi-Arid Region."

Hydrological Processes: An International Journal 22, no. 8: 1093–1106. https://doi.org/10.1002/hyp.6664.

Aminzadeh, M., N. Friedrich, S. Narayanaswamy, K. Madani, and N. Shokri. 2024. "Evaporation Loss From Small Agricultural Reservoirs in a Warming Climate: An Overlooked Component of Water Accounting. Earth's." *Futures* 12, no. 1: e2023EF004050. https://doi.org/10.1029/2023EF004050.

Aminzadeh, M., P. Lehmann, and D. Or. 2018. "Evaporation Suppression and Energy Balance of Water Reservoirs Covered With Self-Assembling Floating Elements." *Hydrology and Earth System Sciences Discussions* 22, no. 7: 4015–4032. https://doi.org/10.5194/hess-22-4015-2018.

Aminzadeh, M., and D. Or. 2014. "Energy Partitioning Dynamics of Drying Terrestrial Surfaces." *Journal of Hydrology* 519: 1257–1270. https://doi.org/10.1016/j.jhydrol.2014.08.037.

Arasteh, P. D., and M. Tajrishy. 2008. "Calibrating Priestley-Taylor Model to Estimate Open Water Evaporation Under Regional Advection Using Volume Balance Method-Case Study: Chahnimeh Reservoir." *Journal of Applied Sciences* 8, no. 22: 4097–4104. https://doi.org/10.3923/jas.2008.4097.4104.

Bakhtiar, M., M. Aminzadeh, M. Taheriyoun, D. Or, and E. Mashayekh. 2022. "Effects of Floating Covers Used for Evaporation Suppression on Reservoir Physical, Chemical and Biological Water Quality Parameters." *Ecohydrology* 15, no. 8: e2470. https://doi.org/10.1002/eco.2470.

Brutsaert, W. 1982. *Evaporation Into the Atmosphere: Theory, History and Applications*. 1st ed. Netherlands: Springer. https://doi.org/10.1007/978-94-017-1497-6.

Cooley, K. R. 1970. "Energy Relationships in the Design of Floating Covers for Evaporation Reduction." *Water Resources Research* 6, no. 3: 717–727. https://doi.org/10.1029/WR006i003p00717.

Cox, C. W. 1999. *Water Supply Enhancement in Cyprus Through Evaporation Reduction: PhD Thesis*. USA: Massachusetts Institute of Technology.

Fekih, M., A. Bourabaa, and S. Mohamed. 2013. "Evaluation of Two Methods for Estimation of Evaporation From Dams Water in Arid and Semi-Arid Areas in Algeria." *International Journal of Application or Innovation in Engineering & Management* 2, no. 1: 2319–4847. https://doi.org/10.5281/zenodo.1077715.

Gallego-Elvira, B., A. Baille, B. Martin-Gorriz, J. Maestre-Valero, and V. M. Alvarez. 2012. "Evaluation of Evaporation Estimation Methods for a Covered Reservoir in a Semi-Arid Climate (South-Eastern Spain)." *Journal of Hydrology* 458: 59–67. https://doi.org/10.1016/j.jhydrol.2012.06.035.

Goldbach, A., and W. Kuttler. 2015. "Turbulent Heat Fluxes Above a Suburban Reservoir: A Case Study From Germany." *Journal of Hydrometeorology* 16, no. 1: 244–260. https://doi.org/10.1175/JHM-D-13-0159.1.

Haghighi, E., and D. Or. 2013. "Evaporation from Porous Surfaces into Turbulent Airflows: Coupling Eddy Characteristics with Pore Scale Vapor Diffusion." *Water Resources Research* 49, no. 12: 8432–8442. https://doi.org/10.1002/2012WR013324.

Helfer, F., F. P. Andutta, J. A. Louzada, H. Zhang, and C. Lemckert. 2018. "Artificial Destratification for Reducing Reservoir Water Evaporation: Is It Effective?" *Lakes & Reservoirs: Research & Management* 23, no. 4: 333–350. https://doi.org/10.1111/lre.12241.

Henderson-Sellers, B. 1986. "Calculating the Surface Energy Balance for Lake and Reservoir Modeling: A Review." *Reviews of Geophysics* 24, no. 3: 625–649. https://doi.org/10.1029/RG024i003p00625.

Hojjati, E., G. Mahtabi, F. Taran, and O. Kisi. 2020. "Estimating Evaporation From Reservoirs Using Energy Budget and Empirical Methods: Alavian Dam Reservoir, NW Iran." *Italian Journal of Agrometeorology* 2: 19–34. https://doi.org/10.13128/ijam-1033.

Kalma, J. D., and D. L. B. Jupp. 1990. "Estimating Evaporation From Pasture Using Infrared Thermometry: Evaluation of a One-Layer Resistance Model." *Agricultural and Forest Meteorology* 51, no. 3–4: 223–246. https://doi.org/10.1016/0168-1923(90)90110-R.

Lehmann, P., M. Aminzadeh, and D. Or. 2019. "Evaporation Suppression From Water Bodies Using Floating Covers: Laboratory Studies of Cover Type, Wind and Radiation Effects." *Water Resources Research* 55, no. 6: 4839–4853. https://doi.org/10.1029/2018WR024489.

Majidi, M., A. Alizadeh, A. Farid, and M. Vazifedoust. 2015. "Estimating Evaporation From Lakes and Reservoirs Under Limited Data Condition in a Semi-Arid Region." *Water Resources Management* 29: 3711–3733. https://doi.org/10.1007/s11269-015-1025-8.

McGloin, R., H. McGowan, D. McJannet, F. Cook, A. Sogachev, and S. Burn. 2014. "Quantification of Surface Energy Fluxes From a Small Water Body Using Scintillometry and Eddy Covariance." *Water Resources Research* 50, no. 1: 494–513. https://doi.org/10.1002/2013WR013899.

McJannet, D. L., F. J. Cook, R. P. McGloin, H. A. McGowan, and S. Burn. 2011. "Estimation of Evaporation and Sensible Heat Flux From Open Water Using a Large-Aperture Scintillometer." *Water Resources Research* 47, no. 5: W05545. https://doi.org/10.1029/2010WR010155.

Millán, M., M. J. Estrela, and V. Caselles. 1995. "Torrential Precipitations on the Spanish East Coast: The Role of the Mediterranean Sea Surface Temperature." *Atmospheric Research* 36, no. 1–2: 1–16. https://doi.org/10.1016/0169-8095(94)00048-I.

Moreo, M. T., and A. Swancar. 2013. "Evaporation From Lake Mead, Nevada and Arizona, March 2010 Through February 2012." *US Geological Survey Scientific Investigations Report* 40: 5229. https://doi.org/10.3133/sir20135229.

Nordbo, A., S. Launiainen, I. Mammarella, et al. 2011. "Long-Term Energy Flux Measurements and Energy Balance Over a Small Boreal Lake Using Eddy Covariance Technique." *Journal of Geophysical Research—Atmospheres* 116, no. D2: D02119. https://doi.org/10.1029/2010JD014542.

Priestley, C. H. B., and R. J. Taylor. 1972. "On the Assessment of Surface Heat Flux and Evaporation Using Large-Scale Parameters." *Monthly Weather Review* 100, no. 2: 81–92. https://doi.org/10.1175/1520-0493(1972)100%3C0081:OTAOSH%3E2.3.CO;2.

Rachid, N., N. Issam, B. Abdelkrim, A. Abdelhamid, and H. Amina. 2022. "Pond Energy Dynamics, Evaporation Rate and Ensemble Deep Learning Evaporation Prediction: Case Study of the Thomas Pond—Brenne Natural Regional Park (France)." *Water* 14, no. 6: 923. https://doi.org/10.3390/w14060923.

Rezazadeh, A., P. Akbarzadeh, and M. Aminzadeh. 2020a. "Modelling and Experimental Investigation of the Evaporation Suppression Using Floating Covers in the Presence of Surface Flows." *Amirkabir Journal of Mechanical Engineering* 53, no. 1: 1–3. https://doi.org/10.22060/mej.2019.15515.6145.

Rezazadeh, A., P. Akbarzadeh, and M. Aminzadeh. 2020b. "The Effect of Floating Balls Density on Evaporation Suppression of Water Reservoirs in the Presence of Surface Flows." *Journal of Hydrology* 591: 125323. https://doi.org/10.1016/j.jhydrol.2020.125323.

Rohli, R. V., S. A. Hsu, B. M. Lofgren, and M. R. Binkley. 2004. "Bowen Ratio Estimates Over Lake Erie." *Journal of Great Lakes Research* 30, no. 2: 241–251. https://doi.org/10.1016/S0380-1330(04)70342-1.

Sattari, M. T., V. Ahmadifar, R. Delirhasannia, and H. Apaydín. 2021. "Estimation of the Pan Evaporation Coefficient in Cold and Dry Climate Conditions via the M5 Regression Tree Model." *Atmosfera* 34, no. 3: 289–300. https://doi.org/10.20937/ATM.52777.

Sherman, B., C. Lemckert, and H. Zhang. 2010. "The Impact of Artificial Destratification on Reservoir Evaporation." Urban Water Security Research Alliance Technical Report No. 35, December (2010).

Sun, J., W. Hu, N. A. Wang, et al. 2018. “Eddy Covariance Measurements of Water Vapor and Energy Flux Over a Lake in the Badain Jaran Desert, China.” *Journal of Arid Land* 10: 517–533. https://doi.org/10.1007/s40333-018-0057-3.

Tanny, J., S. Cohen, D. Berger, et al. 2011. “Evaporation From a Reservoir With Fluctuating Water Level: Correcting for Limited Fetch.” *Journal of Hydrology* 404, no. 3–4: 146–156. https://doi.org/10.1016/j.jhydrol.2007.12.012.

Van Dijk, M., and S. J. Van Vuuren. 2009. “Destratification Induced by Bubble Plumes as a Means to Reduce Evaporation From Open Impoundments.” *Water SA* 35, no. 2: 158–167. http://hdl.handle.net/2263/13540.

Verburg, P., and J. P. Antenucci. 2010. “Persistent Unstable Atmospheric Boundary Layer Enhances Sensible and Latent Heat Loss in a Tropical Great Lake, Lake Tanganyika.” *Journal of Geophysical Research-Atmospheres* 115, no. D11: D11109. https://doi.org/10.1029/2009JD012839.

Yang, F., and K. M. Lau. 2004. “Trend and Variability of China Precipitation in Spring and Summer: Linkage to Sea-Surface Temperatures.” *International Journal of Climatology* 24, no. 13: 1625–1644. https://doi.org/10.1002/joc.1094.

Yang, Y., and M. L. Roderick. 2019. “Radiation, Surface Temperature and Evaporation Over Wet Surfaces.” *Quarterly Journal of the Royal Meteorological Society* 145, no. 720: 1118–1129. https://doi.org/10.1002/qj.3481.

Yao, Y., S. Liang, J. Cheng, et al. 2013. “MODIS-Driven Estimation of Terrestrial Latent Heat Flux in China Based on a Modified Priestley–Taylor Algorithm.” *Agricultural and Forest Meteorology* 171: 187–202. https://doi.org/10.1016/j.agrformet.2012.11.016.

Yao, Y., S. Liang, S. Zhao, et al. 2014. “Validation and Application of the Modified Satellite-Based Priestley-Taylor Algorithm for Mapping Terrestrial Evapotranspiration.” *Remote Sensing* 6, no. 1: 880–904. https://doi.org/10.3390/rs6010880.

Youssef, Y. W., and A. Khodzinskaya. 2019. “A Review of Evaporation Reduction Methods From Water Surfaces.” *E3S Web of Conferences* 97: 5044. https://doi.org/10.1051/E3SCONF/20199705044.

Appendix A

Changes in relative humidity and air temperature at different heights above the water surface for six different states of wind speed are shown in Figures A1 and A2, respectively.

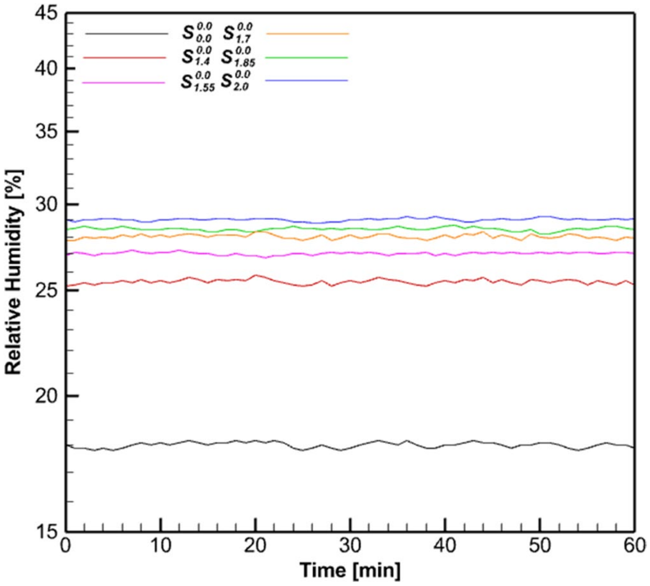

FIGURE A1 | Changes in relative air humidity for six different states of wind speed cases $S^{0.0}_{0.0}$, $S^{0.0}_{1.4}$, $S^{0.0}_{1.55}$, $S^{0.0}_{1.7}$, $S^{0.0}_{1.85}$ and $S^{0.0}_{2.0}$.

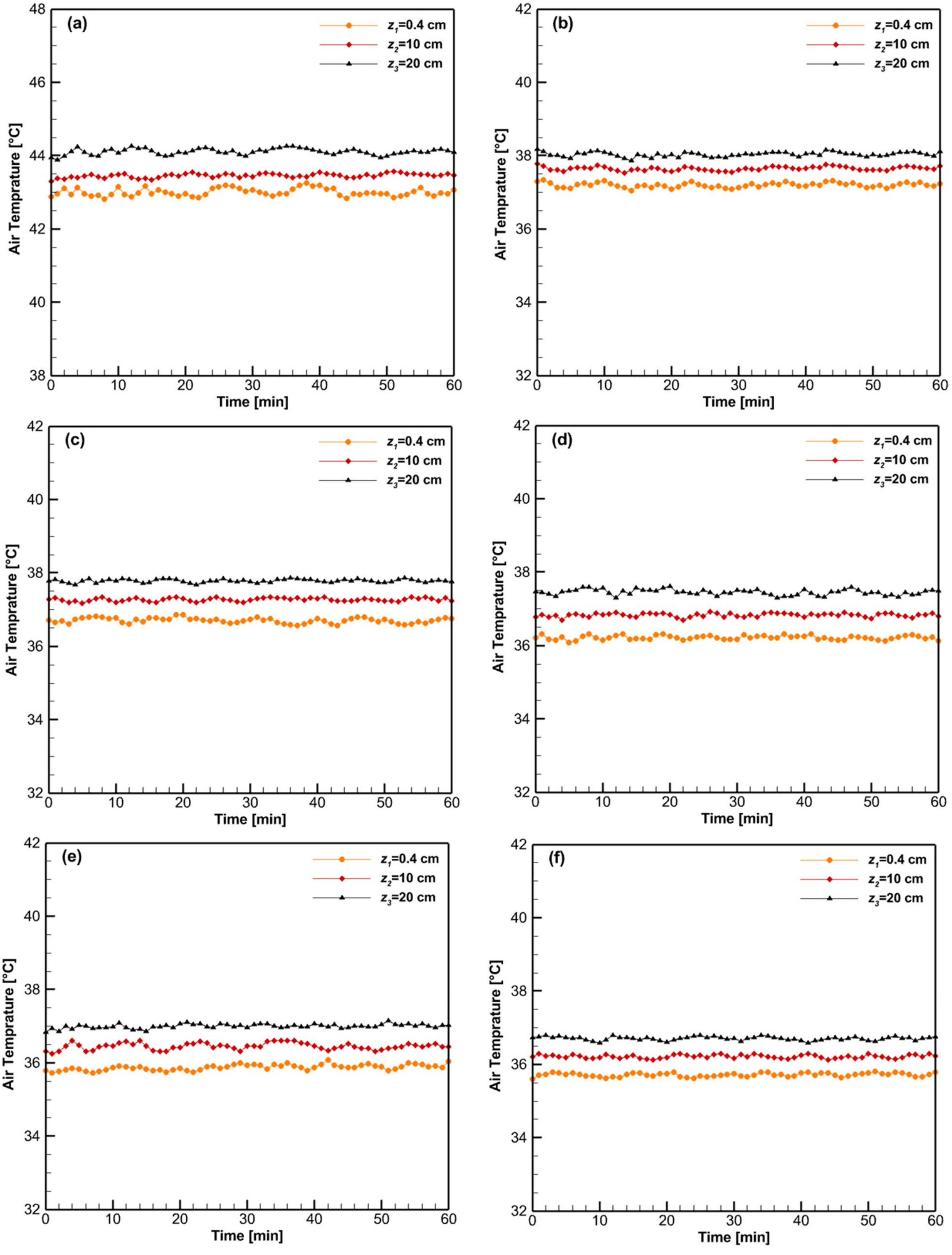

FIGURE A2 | Changes in air temperature at different heights above the water surface for six different states of wind speed: (a) $S^{0.0}_{0.0}$, (b) $S^{0.0}_{1.4}$, (c) $S^{0.0}_{1.55}$. (d) $S^{0.0}_{1.7}$, (e) $S^{0.0}_{1.85}$ and (f) $S^{0.0}_{2.0}$.

Appendix B

This section presents the standard error values, calculated by dividing the standard deviation by the square root of the number of measurements (in this study, each test is conducted three times), as the uncertainty for sensible heat flux (Table B1), and the Bowen ratio (Table B2) under tailwind and headwind conditions.

TABLE B1 | The uncertainty for sensible heat flux [W m^{-2}] based on standard error values.

	[I min^{-1}]	U_a [m s^{-1}]					
Test scenarios	**q**	**$U_a = 0.0$**	**$U_a = 1.4$**	**$U_a = 1.55$**	**$U_a = 1.7$**	**$U_a = 1.85$**	**$U_a = 2.0$**
Tailwind	0.0	± 1.78	± 1.71	± 1.80	± 1.95	± 1.97	± 1.74
	1.0	± 2.05	± 1.81	± 2.07	± 1.64	± 1.87	± 2.12
	2.5	± 1.52	± 1.45	± 1.62	± 1.75	± 1.69	± 2.00
	4.5	± 2.05	± 1.70	± 1.81	± 2.62	± 2.03	± 1.62
	5.5	± 1.80	± 1.90	± 1.70	± 1.82	± 1.74	± 1.91
	7.5	± 1.46	± 1.58	± 1.78	± 1.90	± 2.09	± 2.79
	8.5	± 1.66	± 1.70	± 1.51	± 1.60	± 2.03	± 1.95
	10.5	± 1.90	± 1.80	± 1.73	± 1.65	± 1.55	± 1.61
Headwind	0.0	± 1.78	± 1.45	± 3.25	± 1.48	± 1.99	± 4.29
	1.0	± 2.05	± 1.99	± 2.75	± 1.99	± 2.01	± 2.00
	2.5	± 1.52	± 1.56	± 2.94	± 1.97	± 1.63	± 1.75
	4.5	± 2.05	± 1.96	± 2.39	± 2.25	± 2.15	± 2.32
	5.5	± 1.80	± 1.90	± 1.87	± 1.80	± 1.71	± 1.90
	7.5	± 1.46	± 1.72	± 2.50	± 1.55	± 1.70	± 1.86
	8.5	± 1.66	± 1.67	± 2.58	± 1.82	± 1.88	± 2.17
	10.5	± 1.90	± 1.90	± 2.75	± 1.93	± 1.45	± 1.91

TABLE B2 | The uncertainty for the Bowen ratio ($\beta_{Ex} = H_{Ex} / LE_{Ex}$) based on standard error values.

	[I min^{-1}]	U_a [m s^{-1}]					
Test scenarios	**q**	**$U_a = 0.0$**	**$U_a = 1.4$**	**$U_a = 1.55$**	**$U_a = 1.7$**	**$U_a = 1.85$**	**$U_a = 2.0$**
Tailwind	0.0	± 0.0066	± 0.0065	± 0.0066	± 0.0049	± 0.0062	± 0.0047
	1.0	± 0.0059	± 0.0048	± 0.0078	± 0.0047	± 0.0051	± 0.0068
	2.5	± 0.0105	± 0.0052	± 0.0067	± 0.0073	± 0.0066	± 0.0067
	4.5	± 0.0130	± 0.0072	± 0.0069	± 0.0087	± 0.0065	± 0.0054
	5.5	± 0.0050	± 0.0059	± 0.0074	± 0.0069	± 0.0055	± 0.0049
	7.5	± 0.0035	± 0.0070	± 0.0078	± 0.0049	± 0.0071	± 0.0072
	8.5	± 0.0042	± 0.0086	± 0.0080	± 0.0044	± 0.0063	± 0.0049
	10.5	± 0.0064	± 0.0054	± 0.0060	± 0.0043	± 0.0049	± 0.0036
Headwind	0.0	± 0.0066	± 0.0037	± 0.0088	± 0.0052	± 0.0051	± 0.0115
	1.0	± 0.0059	± 0.0063	± 0.0096	± 0.0065	± 0.0042	± 0.0047
	2.5	± 0.0105	± 0.0035	± 0.0098	± 0.0068	± 0.0042	± 0.0054
	4.5	± 0.0130	± 0.0053	± 0.0082	± 0.0068	± 0.0062	± 0.0073
	5.5	± 0.0050	± 0.0054	± 0.0062	± 0.0047	± 0.0046	± 0.0054
	7.5	± 0.0035	± 0.0061	± 0.0095	± 0.0040	± 0.0060	± 0.0055
	8.5	± 0.0042	± 0.0064	± 0.0055	± 0.0058	± 0.0059	± 0.0063
	10.5	± 0.0064	± 0.0047	± 0.0076	± 0.0064	± 0.0033	± 0.0048

Appendix C

In Figure C1, temperature changes of six layers of water for tailwind conditions are introduced in different states of wind speed and water surface flow. In Figure C2, these temperature changes are expressed for headwind conditions in other states.

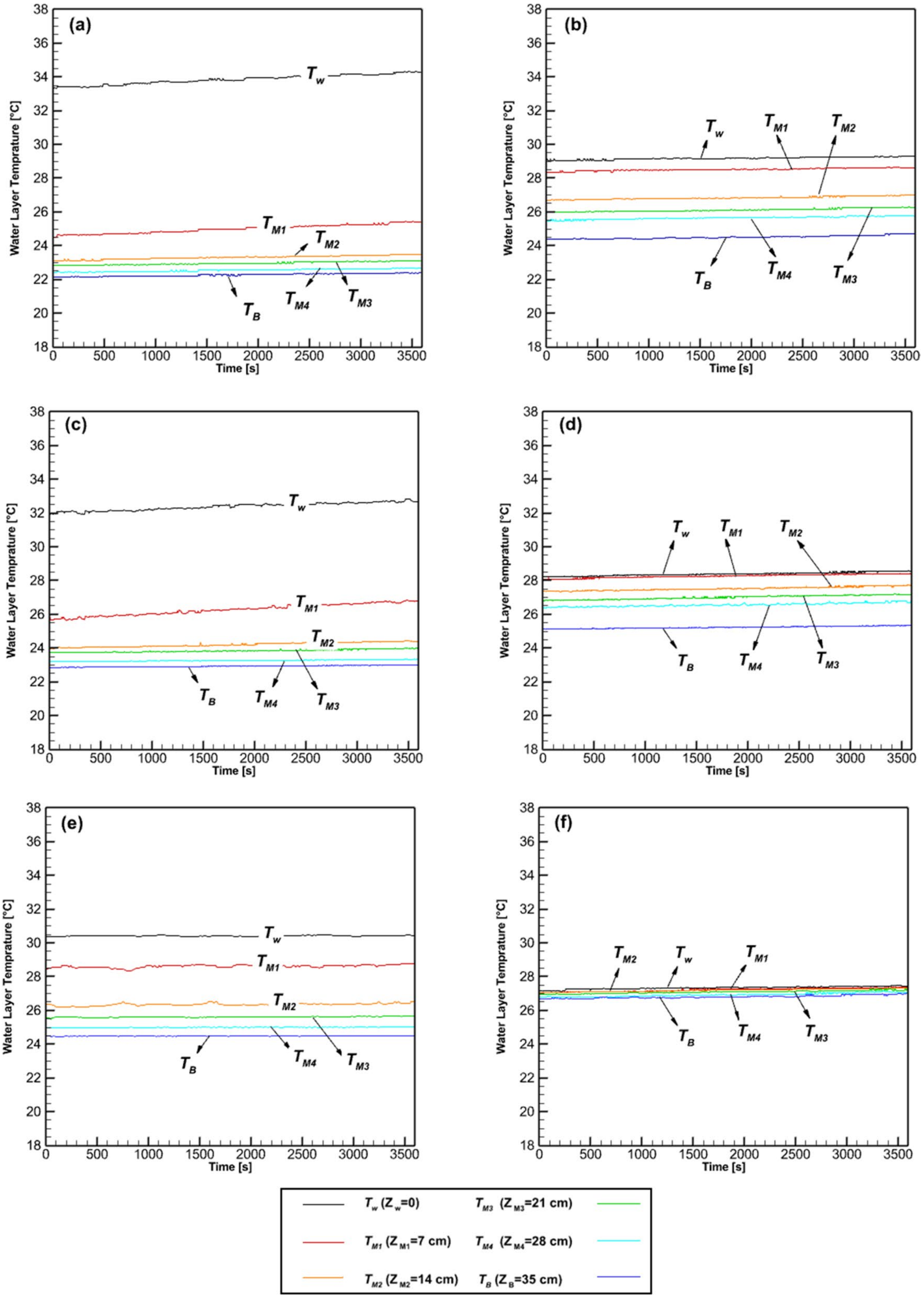

FIGURE C1 | The temperature changes in six water layers for the tailwind cases: (a) $S^{0.0}_{0.0}$. (b) $S^{0.0}_{2.0}$. (c) $S^{4.5}_{0.0}$. (d) $S^{4.5}_{2.0}$. (e) $S^{10.5}_{0.0}$. (f) $S^{10.5}_{2.0}$.

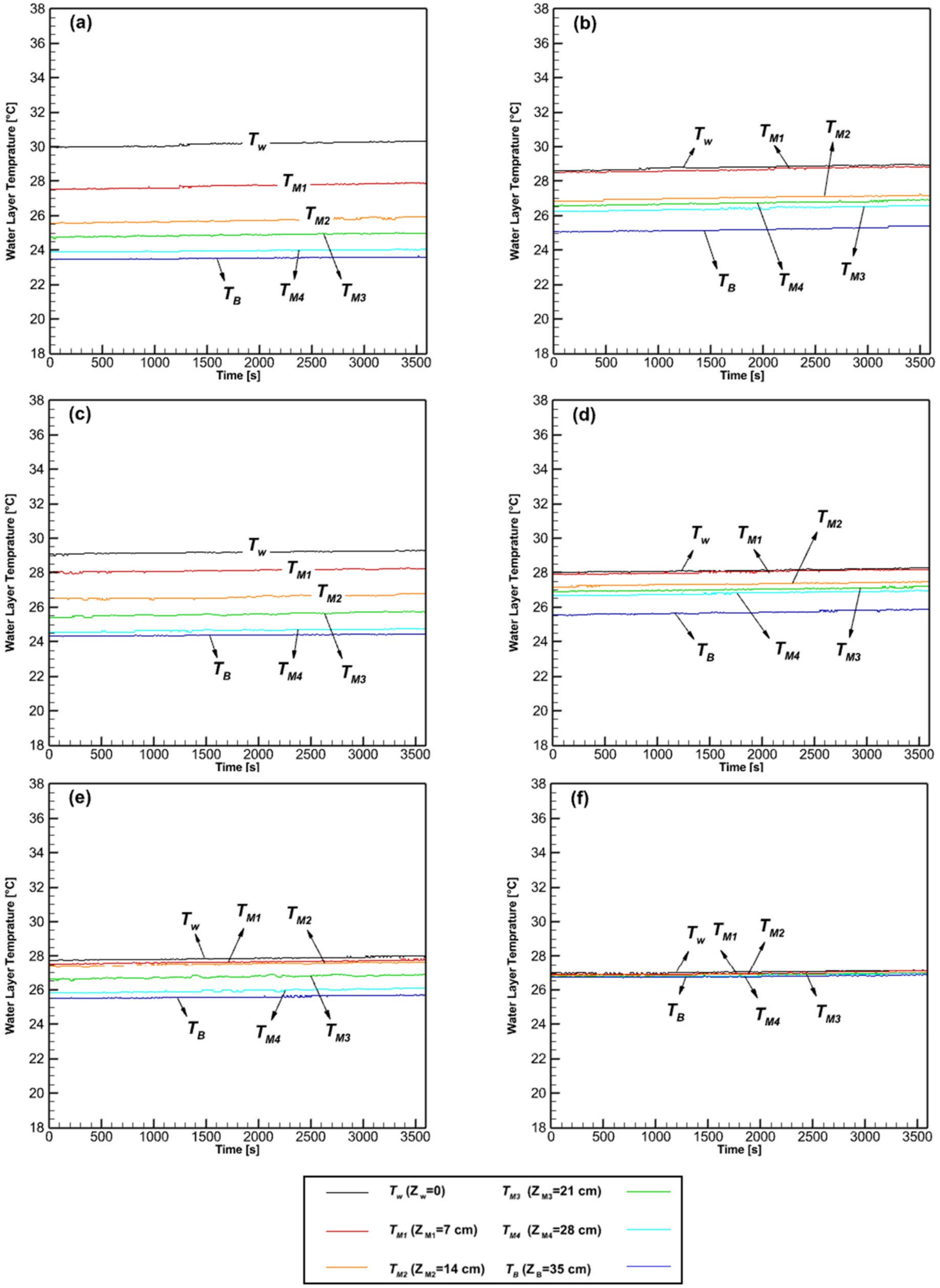

FIGURE C2 | The temperature changes in six water layers for the headwind cases: (a) $S^{1.0}_{1.4}$, (b) $S^{1.0}_{2.0}$, (c) $S^{4.5}_{1.4}$, (d) $S^{4.5}_{2.0}$, (e) $S^{10.5}_{1.4}$, (f) $S^{10.5}_{2.0}$.

Appendix D

The water energy balance based on a simple representation of surface and lateral heat fluxes provides a theoretical basis for interpreting experimental findings. The model investigates the contribution of water surface flows and latent, sensible, and radiative fluxes in changing water body energy storage based on Equation (D1) (Rezazadeh, Akbarzadeh, and Aminzadeh 2020a, 2020b; Fekih, Bourabaa, and Mohamed 2013; Tanny et al. 2011; Cooley 1970; Sattari et al. 2021; Lehmann, Aminzadeh, and Or 2019):

$$H_{EB} = R_n - LE - \Delta S + Q_V + Q_{\text{wall}} \tag{D1}$$

In this analysis, R_n denotes the net radiation, $L = \lambda / \left(3.6 \times 10^3 A_s\right)$ is a conversion coefficient $\left[\text{J h g}^{-1}\ \text{m}^{-2}\text{s}^{-1}\right]$ to link evaporation rate ($E\ \left[\text{g h}^{-1}\right]$) with latent heat flux (LE) in which A_s represents the area of the water's surface $\left[\text{m}^2\right]$, and λ [J g^{-1}] is the latent heat of water vaporisation.

ΔS captures the change in water energy storage, H_{EB} quantifies the sensible heat flux, Q_V indicates the heat transfer rate through the flow of water (applicable when the reservoir has an inlet and outlet flow), and Q_{wall} captures the heat exchanged through the walls of the reservoir. In Equation (D1), all quantities are expressed in the unit of watt per square meter $\left[\text{W m}^{-2}\right]$. The difference between the incoming and outgoing short- and longwave radiation fluxes, known as the net radiation (R_n), is captured by Equation (D2) (Gallego-Elvira et al. 2012; Henderson-Sellers 1986):

$$R_n = \left(1 - r_w\right) S + \varepsilon_w \sigma \left(\varepsilon_a {T_a}^4 - {T_{ws}}^4\right) \tag{D2}$$

Where r_w (~ 0.05) is the reflection coefficient of shortwave (albedo), $\varepsilon_w = 0.95$ is the emissivity of water, S is the incoming shortwave radiation, T_{ws} is the temperature of the water surface, T_a is the air temperature, $\sigma = 5.67 \times 10^{-8}$ W m^{-2}K^{-4} is the Stefan-Boltzman constant. The atmospheric emissivity (ε_a) changes with air temperature and actual vapour pressure (e_a) as follows (Brutsaert 1982):

$$\varepsilon_a = 1.24\left(e_a / T_a\right)^{\frac{1}{7}} \tag{D3}$$

The change in water energy storage, ΔS can be obtained as follows (Moreo and Swancar 2013; Hojjati et al. 2020; Ali, Ghosh, and Singh 2008):

$$\Delta S = \rho_w c_w \sum_{j=1}^{N} Z_j \left(\Delta T_{wj} / \Delta t\right) \tag{D4}$$

Where, c_w denotes the heat capacity of water $\left[\text{kJ kg}^{-1}\text{K}^{-1}\right]$, Z_j stands for the depth of each water layer (in this study, water temperature is measured in six different layers at depths of $Z_w = 0$, $Z_{M1} = 7$, $Z_{M2} = 14$, $Z_{M3} = 21$, $Z_{M4} = 28$, and $Z_B = 35$ cm from the free surface of the basin), and ΔT_{wj} [°C] represents the change in water temperature for each layer during a given time step (Δt). In a reservoir where water inflow and outflow are present, the net advected heat into the reservoir can be described using the volume-weighted heat content of the water inflows and outflows, as explained in the following (Moreo and Swancar 2013; Rezazadeh, Akbarzadeh, and Aminzadeh 2020a, 2020b):

$$Q_V = \frac{\sum_i c_w V_i \left(T_i - \overline{T}\right) - \sum_o c_w V_o \left(T_o - \overline{T}\right)}{A_s \Delta t} \tag{D5}$$

Where V_i and V_o $\left[\text{m}^3\right]$ represent the volume of water input and output during the test, respectively. T_i and T_o represent the mean temperatures of the inflows and outflows, respectively. The parameter $\overline{T}$ represents the mean temperature of the basin. In the present experiments, the water is circulated by a pump in a closed system. As a result, the temperature difference between the inlet and outlet water flows rapidly adjusts to a value close to zero at the beginning of each experiment. This adjustment allows the heat transfer rate (Q_V) to approach zero. Finally, the heat exchanges with the surroundings through the reservoir walls (Q_{wall}) can be determined as follows (Rezazadeh, Akbarzadeh, and Aminzadeh 2020a, 2020b):

$$Q_{\text{wall}} = -k\left(\Delta T_w / \Delta x\right) \tag{D6}$$

Where k is the thermal conductivity of the basin walls, ΔT_w is the temperature difference between the two sides of the basin wall, and Δx is the wall thickness. Based on the reservoir's density, the thermal conductivity for the polyethylene basin in the present study is estimated as 0.38 W m^{-1}K^{-1}.

Appendix E

Table E1 displays the relative error [%] between the heat flux sensor data and the results obtained from the energy balance equation for calculating the sensible heat flux.

TABLE E1 | The relative error [%] values obtained by comparing the experimental data with the results obtained from the energy balance equation for calculating the sensible heat flux.

	$[\mathrm{I\ min^{-1}}]$	$U_a\ [\mathrm{m}\ s^{-1}]$					
Test scenarios	q	$U_a = 0.0$	$U_a = 1.4$	$U_a = 1.55$	$U_a = 1.7$	$U_a = 1.85$	$U_a = 2.0$
Tailwind	0.0	0.073	0.066	0.071	0.072	0.0052	0.050
	1.0	0.060	0.091	0.053	0.088	0.0072	0.050
	2.5	0.031	0.089	0.060	0.068	0.058	0.048
	4.5	0.069	0.049	0.057	0.056	0.038	0.064
	5.5	0.027	0.048	0.046	0.038	0.028	0.046
	7.5	0.053	0.058	0.055	0.037	0.028	0.053
	8.5	0.027	0.055	0.053	0.044	0.046	0.036
	10.5	0.049	0.045	0.044	0.052	0.028	0.050
Headwind	0.0	0.073	0.066	0.071	0.072	0.052	0.050
	1.0	0.060	0.089	0.050	0.049	0.082	0.055
	2.5	0.031	0.039	0.085	0.082	0.080	0.045
	4.5	0.069	0.084	0.039	0.080	0.078	0.038
	5.5	0.027	0.082	0.047	0.078	0.076	0.027
	7.5	0.053	0.063	0.045	0.036	0.075	0.073
	8.5	0.027	0.045	0.076	0.059	0.073	0.049
	10.5	0.049	0.044	0.035	0.019	0.071	0.026